East European Journal of Physics. 2. 302-318 (2026)
DOI:10.26565/2312-4334-2026-2-32 ISSN 2312-4334

ANALYSIS OF THERMO-MAGNETIC CASSON HYBRID NANOFLUID FLOW OVER A POROUS STRETCHING SHEET CONSIDERING CHEMICAL REACTION USING RSM

Esara Sivasankar[1], M. Sreedhar Babu[1]*, S. Vijaya Kumar Varma[2]
[1]*Department of Applied Mathematics, Yogi Vemana University, Kadapa, Andhra Pradesh, 516005, India*
[2]*Department of Mathematics, School of Applied Sciences, REVA Research Center, REVA University, Bengaluru, Karnataka, 560064, India*
**Corresponding Author email: [*]msreedharyvu@gmail.com*
E-mail: [1]sivaesara1234@gmail.com,[2]vijayakumar.varma@reva.edu.in
Received February 4, 2026; revised March 31, 2026; accepted April 2, 2026

Thermophysical analysis of heat and mass transmission has many potential uses in solar collectors, chemical reactors, medicinal devices, and sophisticated cooling systems, among other applications. Owing to this incentive, the present work often employs response surface methodology for heat and mass transfer analysis of a Casson hybrid nanofluid over a permeable stretching sheet with convective and radiative effects. The control system of the PDEs defining the developed model is transformed into a coupled set of nonlinear ODEs by applying appropriate similarity transformations. The shooting method, implemented with MATLAB's BVP4c solver, is used to numerically integrate these simplified equations. Using tabulated data and graphical representations, the effects of relevant physical parameters on the distributions of velocity, temperature, and concentration are systematically examined. Additionally, Response Surface Methodology is used to statistically evaluate key response variables across a broad range of governing parameters, such as the skin-friction coefficient, heat, and mass-transfer rates. The findings show that increasing the Casson parameter reduces the temperature profile because the fluid's effective yield stress decreases. Furthermore, due to increased Lorentz forces, a higher magnetic field considerably reduces fluid velocity. Additionally, it has been observed that an increased solid volume fraction raises the nanofluid's temperature due to enhanced thermal conductivity. The statistical analysis indicates that the mass-transfer accuracy for the derived mathematical model in kerosene is 99.85%.
Keywords: *Casson Hybrid nanofluid; MHD; Porous stretching sheet; Chemical Reaction; Response Surface Method (RSM)*
PACS: 44.30 +v, 44.05 +e, 44.20.+b, 45.65.cb

INTRODUCTION

A stretching sheet is a theoretical and practical concept in fluid mechanics where a flexible sheet is continuously stretched in a particular direction, typically in an unbounded fluid medium. Also, stretching sheets are studied to improve heat transfer efficiency in cooling systems, in energy-efficient coatings, and smart materials. Furthermore, to boost the heat transfer, the researchers added the nanoparticles to the conventional fluids, such as nanofluid, first coined. The dispersion of a single type of nanoparticle in a base fluid is often insufficient to attain the enhanced thermal performance required in advanced heat transfer applications. To overcome this limitation, a mixture of two distinct nanoparticles suspended in a base fluid referred to as a hnf has been introduced to improve thermophysical properties. The influence of magnetohydrodynamics (MHD) on nanofluid flow plays a crucial role in controlling fluid motion and heat transfer behavior, and its significance has been demonstrated across numerous practical engineering and industrial applications. In this area of research, Crane [1] was the first to present the fundamental two-dimensional boundary layer solution for flow induced by a stretching surface. Subsequently, Khashi'ie et al. [2] conducted a numerical study on the heat transfer behavior of an MHD hybrid nanofluid (Al_2O_3/H_2O) over a stretching sheet. Shoaib et al. [3] analyzed the influence of system rotation on magnetized hybrid nanofluid flow past an extending surface, while more recently, Sreedevi et al. [4] explored the transient magnetohydrodynamic heat and mass transfer characteristics of hybrid nanofluid flow over a stretching sheet. The impact of thermal radiation on magnetohydrodynamic hybrid nanofluid flow over a stretched wedge was investigated by Waini et al. [5], underscoring the growing significance of radiative effects in hybrid nanofluid transport. The behavior of unstable magnetohydrodynamic hybrid nanofluid flow over a stretching surface was examined by Santhi et al. [6].

The function of velocity slip in both steady and unsteady flow regimes across a stretching sheet. Dinarvand et al. [7] conducted a detailed study on the flow and thermal characteristics near the stagnation region of a shrinking porous surface. Haq et al. [8] explored the heat transfer performance of a Newtonian hybrid nanofluid containing Cu and Al_2O_3 nanoparticles over a stretching sheet. Shah et al. [9] assessed the thermal efficiency of magnetohydrodynamic hybrid nanofluid flow along a stretching surface. Elattar et al. [10] analyzed the flow behavior of an electrically conducting hybrid nanofluid over a thin, non-porous stretching sheet. Farooq et al. [11] investigated the coupled influence of surface permeability, internal heat source or sink, and thermal radiation on magnetohydrodynamic nanofluid flow over an inclined stretching surface. Non-Newtonian fluids such as Casson fluids are characterized by the presence of a yield stress, exhibiting solid-like behavior until a critical stress limit is exceeded. These fluids are widely employed to represent practical materials including blood, printing inks, and food products such as tomato paste. Consequently, considerable research attention has been devoted to Casson nanofluid flow over stretching surfaces. In this sense, under constant

Cite as: E. Sivasankar, M.S. Babu, S.V.K. Varma, East Eur. J. Phys. 2, 302 (2026), https://doi.org/10.26565/2312-4334-2026-2-32

boundary layer conditions, Bhattacharyya [12] investigated the velocity and thermal properties of Casson fluid flow toward a stretching sheet. The effects of slip velocity and viscous dissipation were taken into account when Aly et al. [13] theoretically and statistically investigated magnetohydrodynamic stagnation point flow of a hybrid nanofluid across a stretching surface.

Jamaludin et al. [14] studied the magnetohydrodynamic stagnation-point flow of a hybrid nanofluid over a permeable stretched sheet. Nandi et al. [15] analyzed unsteady magnetohydrodynamic mixed convection stagnation-point flow of a hybrid nanofluid within a homogeneous porous medium over an exponentially stretching surface. Rashid et al. [16] studied the flow characteristics of a hybrid nanofluid containing alumina and silver nanoparticles past a stretching sheet. Khan et al. [17] examined boundary-layer flow and heat transfer behavior of a water-based hybrid nanofluid over a stretching surface. Ghasemi et al. [18] explored the simultaneous influence of thermal radiation and an applied magnetic field on nanofluid flow along a stretching sheet. While Zainal et al. [19] examined the continuous flow of an Al2O3–Cu/water hybrid nanofluid under a magnetic influence over stretching and shrinking surfaces, Ali et al. [20] examined the flow dynamics of a magnetically driven hybrid nanofluid over a stretching sheet. Magnetohydrodynamic nanofluid flow over a porous stretched surface was investigated by Neethu et al. [21]. The impact of a chemical reaction on the flow behavior of a Casson nanofluid was investigated by Nadeem et al. [22]. Magnetohydrodynamic Casson nanofluid flow across a permeable stretching surface was assessed by Qing et al. [23]. Khan et al. [24] examined the behavior of unsteady mass and heat transfer while accounting for chemical processes. Dahab et al. [25] investigated how Casson nanofluid flow over a stretched sheet was affected by wall suction and injection. A nonlinear, surface-induced, two-dimensional Casson hybrid nanofluid flow was investigated by Hameed et al. [26]. Meenakumari et al. [27] investigated the mass and heat transfer properties of a Casson nanofluid flow over an inclined, permeable stretched sheet.

The coupled effects of a Casson hybrid nanofluid moving over a permeable stretching surface, while accounting for magnetic field effects, internal heat generation, viscosity dissipation, and chemical reactions, have not yet been described, according to a careful review of previous research. The present work investigates the influence of governing parameters on the flow of a thermally magnetized Casson hybrid nanofluid over a porous stretching sheet, while incorporating the effects of viscous dissipation and chemical reactions to address the identified research gap. The hybrid nanofluid is formulated by dispersing alumina (Al_2O_3) and cobalt (Co) nanoparticles into a kerosene–water base fluid. Because of its improved thermal conductivity, magnetic responsiveness, and reactive-transport properties, this combination has garnered increasing attention and is appropriate for advanced engineering and industrial heat and mass-transfer applications. Al_2O_3 and Co nanoparticles combined with a water hybrid nanofluid base fluid are used in biomedical cooling systems, microchannel heat sinks for quick heat dissipation, and to enhance solar energy absorption and thermal transfer, particularly in the presence of varying sun intensities. Al_2O_3 and Co nanoparticles are combined with kerosene as the base fluid. Al_2O_3 enhances thermal stability, while Co could assist with combustion that is magnetically appropriate. This mixed nanofluid can be applied to cloaking or cooling jackets to lessen infrared signatures. The BVP4c package's shooting technique produced the solution. The RSM is also used to analyze mass transfer, shear stress, and heat rate.

MATHEMATICAL FORMULATION

The present study considers a two-dimensional, steady, incompressible flow of an Al_2O_3–cobalt hybrid nanofluid over a porous stretching surface, as illustrated schematically in Figure 1. The composition of the hybrid nanofluid, formed by dispersing two different types of nanoparticles into the base fluids water and kerosene, is summarized in Table 1.

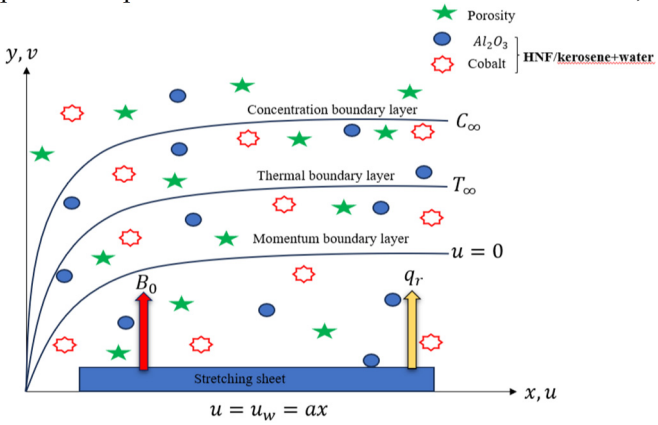

Figure 1. Geometry of the problem

The velocity components in the Cartesian coordinate system are denoted by u and v along the x- and y-directions, respectively. The stretching velocity of the sheet is prescribed as $u_w = ax$, while a uniform transverse magnetic field of strength B_0 is applied. The surface temperature and ambient fluid temperature are represented by T_w, T_∞ respectively, whereas the surface and ambient concentrations are denoted by C_w, C_∞. To describe the flow behavior, the rheological constitutive relation for an isotropic, incompressible Casson fluid is employed and is expressed as follows.

$$\tau_{ij} = \begin{cases} 2(\mu_D + \frac{p_y}{\sqrt{2\pi}})e_{ij}, & \pi > \pi_c, \\ 2(\mu_D + \frac{p_y}{\sqrt{2\pi}})e_{ij}, & \pi < \pi_c, \end{cases}$$

where μ_D represents the fluid's plastic dynamic viscosity, p_y represents the fluid's yield stress, $\pi = e_{ij}e_{ij}$ is the product of the deformation component's rate with itself, and π_c indicates a crucial value of this product using the fluid model as a basis. In this instance, the Casson parameter is $\beta = \mu_D\sqrt{2\pi_c}/p_y$. Furthermore, it provides the formula for the kinematic viscosity of the Casson fluids, which is $\upsilon = \frac{\mu_D}{\rho}\left(1+\frac{1}{\beta}\right)$.

Table 1. Nanofluid and hybrid nanofluid thermophysical characteristics (Tanuja et al. [29])

Properties	Nanofluid	Hybrid nanofluid
Viscosity (μ)	$\mu_{nf} = \frac{1}{(1-\phi_1)^{2.5}}$	$\mu_{hnf} = \frac{\mu_f}{(1-\phi_1)^{2.5}(1-\phi_2)^{2.5}}$
Density (ρ)	$\rho_{nf} = (1-\phi_1)\rho_f + \phi_1\rho_{S1}$	$\rho_{hnf} = (1-\phi_2)\left((1-\phi_1)\rho_f + \phi_1\rho_{S1}\right) + \phi_2\rho_{S2}$
Kinematic viscosity (υ)	$\upsilon_{nf} = \frac{\mu_{nf}}{\rho_{nf}}$	$\upsilon_{hnf} = \frac{\mu_{hnf}}{\rho_{hnf}}$
Heat capacity $\left(\rho c_p\right)$	$\left(\rho c_p\right)_{nf} = (1-\phi_1)\left(\rho c_p\right)_f + \phi_1\left(\rho c_p\right)_{S1}$	$\left(\rho c_p\right)_{hnf} = (1-\phi_2)(1-\phi_1)\left(\rho c_p\right)_f + \phi_1\left(\rho c_p\right)_{S1}(1-\phi_2) + \phi_2\left(\rho c_p\right)_{S2}$
Thermal conductivity (κ)	$\kappa_{nf} = \kappa_f\left[\frac{(s-1)\kappa_f + \kappa_{S1} - (s-1)\phi_1(\kappa_f - \kappa_{S1})}{(s-1)\kappa_f + \kappa_{S1} + \phi_1(\kappa_f - \kappa_{S1})}\right]$	$\kappa_{hnf} = \kappa_{nf}\left[\frac{(s-1)\kappa_{nf} + \kappa_{S2} - (s-1)\phi_2(\kappa_{nf} - \kappa_{S2})}{(s-1)\kappa_{nf} + \kappa_{S2} + \phi_2(\kappa_{nf} - \kappa_{S2})}\right]$
Electrical conductivity (σ)	$\sigma_{nf} = \sigma_f\left[\frac{(s-1)\sigma_f + \sigma_{S1} - (s-1)\phi_1(\sigma_f - \sigma_{S1})}{(s-1)\sigma_f + \sigma_{S1} + \phi_1(\sigma_f - \sigma_{S1})}\right]$	$\sigma_{hnf} = \sigma_{nf}\left[\frac{(s-1)\sigma_{nf} + \sigma_{S2} - (s-1)\phi_2(\sigma_{nf} - \sigma_{S2})}{(s-1)\sigma_{nf} + \sigma_{S2} + \phi_2(\sigma_{nf} - \sigma_{S2})}\right]$
Thermal expansion coefficient (β)	$\beta_{nf} = (1-\phi_1)\beta_f + \phi_1\beta_{S1}$	$\beta_{hnf} = (1-\phi_2)\left((1-\phi_1)\beta_f + \phi_1\beta_{S1}\right) + \phi_2\beta_{S2}$

The governing flow equations are stated as follows (Chandra and Ramasekhar, [28])

$$\frac{\partial u}{\partial x} + \frac{\partial v}{\partial y} = 0 \tag{1}$$

$$u\frac{\partial u}{\partial x} + v\frac{\partial u}{\partial y} = \frac{\mu_{hnf}}{\rho_{hnf}}\left(1+\frac{1}{\beta}\right)\frac{\partial^2 u}{\partial y^2} + g(\beta_c)_{hnf}(C - C_\infty) + g(\beta_t)_{hnf}(T - T_\infty) - \frac{\sigma_{hnf}}{\rho_{hnf}}B_0^2 u - \frac{\mu_{hnf}}{k^*\rho_{hnf}}u \tag{2}$$

$$u\frac{\partial T}{\partial x} + v\frac{\partial T}{\partial y} = \left\{\begin{array}{l} \frac{k_{hnf}}{(\rho c_p)_{hnf}}\frac{\partial^2 T}{\partial y^2} - \frac{1}{(\rho c_p)_{hnf}}\frac{\partial q_r}{\partial y} + \frac{\sigma_{hnf}}{(\rho c_p)_{hnf}}B_0^2 u^2 + \frac{\mu_{hnf}}{k^*(\rho c_p)_{hnf}}u^2 \\ + \frac{\mu_{hnf}}{(\rho c_p)_{hnf}}\left(1+\frac{1}{\beta}\right)\left(\frac{\partial u}{\partial y}\right)^2 + \frac{Q_1}{(\rho c_p)_{hnf}}(T - T_\infty) \end{array}\right\} \tag{3}$$

$$u\frac{\partial C}{\partial x} + v\frac{\partial C}{\partial y} = -k_1(C - C_\infty) + D\frac{\partial^2 C}{\partial y^2} \tag{4}$$

By Rosseland approach, the thermal radiation is considered as follows:

$$q_r = -\frac{4\sigma^* T_\infty^3}{3k^*}\frac{\partial T^4}{\partial y}, \tag{5}$$

From the Taylor's series extension of approximately and T^4 about T_∞ eliminating higher order terms, the following equation is obtained and considered for the study:

$$T^4 = 4T_\infty^3 T - 3T_\infty^4 \tag{6}$$

Putting Eq. (6) in Eq. (3), we get

$$u\frac{\partial T}{\partial x}+v\frac{\partial T}{\partial y}=\left[\begin{array}{l}\dfrac{k_{hnf}}{(\rho c_p)_{hnf}}\dfrac{\partial^2 T}{\partial y^2}-\left(\dfrac{16\sigma^* T_\infty^3}{3k^*}\dfrac{\partial^2 T}{\partial y^2}\right)\dfrac{1}{(\rho c_p)_{hnf}}+\dfrac{\sigma_{hnf}}{(\rho c_p)_{hnf}}B_0^2u^2 \\ +\dfrac{\mu_{hnf}}{k^*(\rho c_p)_{hnf}}u^2+\dfrac{\mu_{hnf}}{(\rho c_p)_{hnf}}\left(1+\dfrac{1}{\beta}\right)\left(\dfrac{\partial u}{\partial y}\right)^2+\dfrac{Q_1}{(\rho c_p)_{hnf}}(T-T_\infty)\end{array}\right] \tag{7}$$

The relevant boundary restrictions are:

$$\left.\begin{array}{l}u=u_w(x)=ax, v=0, \dfrac{\partial C}{\partial y}=\dfrac{q_m}{D}\left(C_f-C\right), \dfrac{\partial T}{\partial y}=\dfrac{q}{k_f}\left(T_f-T\right), as, y\to 0 \\ T=T_f, C=C_f, u\to 0, T\to T_\infty, C\to C_\infty, as, y\to\infty\end{array}\right\} \tag{8}$$

The similarity transformations are defined as:

$$u=axf'(\eta), v=\sqrt{a\upsilon_f}\,f(\eta),\ \theta(\eta)=\frac{T-T_\infty}{T_f-T_\infty},\ \phi(\eta)=\frac{C-C_\infty}{C_f-C_\infty},\ \eta=y\sqrt{\frac{a}{\upsilon_f}} \tag{9}$$

Eqs. (2) to (7) are transformed to dimensional ODEs by using Eq. (9).

$$\left(1+\frac{1}{\beta}\right)f'''-\left(f'\right)^2+ff''+K_6\left(\frac{Gr}{\mathrm{Re}^2}\right)\theta+K_7\left(\frac{Gm}{\mathrm{Re}^2}\right)\phi-\frac{1}{K_2}\left(K_5M+K_1K\right)f'=0 \tag{10}$$

$$\left.\frac{1}{\mathrm{Pr}}\left(\frac{K_4}{K_3}+\frac{4Rd}{3}\frac{1}{K_3}\right)\theta''+f\theta'+\frac{Q}{\mathrm{Pr}\,K_3}\theta+\frac{Ec}{K_3}\left(K_5M+K_1K\right)\left(f'\right)^2+\left(1+\frac{1}{\beta}\right)\frac{K_1}{K_3}Ec\left(f''\right)^2=0\right\} \tag{11}$$

$$\frac{1}{Sc}\phi''+f\phi'-Kr\phi=0\,, \tag{12}$$

where

$$K_1=\frac{\mu_{hnf}}{\mu_f},\ K_2=\frac{\rho_{hnf}}{\rho_f},\ K_3=\frac{\left(\rho c_p\right)_{hnf}}{\left(\rho c_p\right)_f},\ K_4=\frac{k_{hnf}}{k_f},\ K_5=\frac{\sigma_{hnf}}{\sigma_f},\ K_6=\frac{\left(\beta_t\right)_{hnf}}{\left(\beta_t\right)_f},\ K_7=\frac{\left(\beta_c\right)_{hnf}}{\left(\beta_c\right)_f} \tag{13}$$

The reduced boundary conditions are described as:

$$\left.\begin{array}{l}f(0)=0, f'(0)=1,\ \theta'(0)=-B_{i1}(1-\theta(0)),\ \phi'(0)=-B_{i2}(1-\phi(0)),\ at,\ \eta=0 \\ f'(\infty)=0,\ \theta(\infty)=0,\ \phi(\infty)=0,\ at,\ \eta=\infty\end{array}\right\} \tag{14}$$

Table 2. Thermophysical properties of water and Kerosene, Al_2O_3 and Co hybrid nanofluid (Divya *et. al*. [30])

Property	Kerosene	Water	Al_2O_3	Cobalt
Density $\rho\left(kgm^{-3}\right)$	783	997.1	3970	8900
Specific heat $C_p\left(Jkg^{-1}K^{-1}\right)$	2090	4179	765	420
Heat conductivity $k_f\left(Wm^{-1}K^{-1}\right)$	0.145	0.613	40	100
Electrical conductivity $\sigma(\Omega m)^{-1}$	21×10^{-6}	0.05	1×10^{-10}	1.602×10^{7}
Thermal expansion coefficient $\beta\left(K^{-1}\right)$	9.9×10^{-4}	21×10^{-5}	0.00000850	1.3×10^{-5}
Pr (Prandtl number)	21	6.8		

Dimensionless parameters

$$M=\frac{\sigma_f B_0^2}{\rho_f a},\quad \mathrm{Pr}=\frac{\mu_f(c_p)_f}{k_f},\quad Rd=\frac{4\sigma^* T_\infty^3}{k^* k_f},\quad Ec=\frac{a^2x^2}{(c_p)_f(T_f-T_\infty)},\quad K=\frac{\upsilon_f}{ak^*},\quad Q=\frac{Q_1\upsilon_f}{k_f}, Sc=\frac{\upsilon_f}{D},\quad B_{i1}=\frac{q}{k_f}\sqrt{\frac{\upsilon_f}{a}},$$

$$B_{i2}=\frac{q_m}{D}\sqrt{\frac{\upsilon_f}{a}},\ Kr=\frac{k_1}{a},\ Gr=\frac{g(\beta_t)(T_f-T_\infty)x^3}{\upsilon_f^{\,2}},\ Gm=\frac{g(\beta_c)(C_f-C_\infty)x^3}{\upsilon_f^{\,2}},\ \mathrm{Re}=\frac{ax^2}{\upsilon_f}$$

Derived quantities

The skin friction coefficient (Cf), Nusselt number (Nu) and Sherwood number (Sh) transferred in their dimensional form are written as

$$Cf = \frac{\tau_w}{\rho_f u_w^2} \tag{15}$$

Where, shear stress τ_w is $\tau_w = \mu_{hnf} \left.\frac{\partial u}{\partial y}\right|_{y=o}$

$$Nu = \frac{x q_w}{k_f \left(T_w - T_\infty\right)} \tag{16}$$

Where, the heat flux q_w is $q_w = -k_{hnf} \left.\frac{\partial T}{\partial y}\right|_{y=o}$

$$Sh = \frac{x q_m}{D_B \left(C_w - C_\infty\right)} \tag{17}$$

Where, mass flux q_m is $q_m = -D_B \left.\frac{\partial C}{\partial y}\right|_{y=o}$

The non-dimensional form of equations (15-17) is converted to

$$\left.\begin{aligned} \mathrm{Re}_r^{1/2} C_f &= Cf = K_1 f''(0) \\ \mathrm{Re}_r^{-1/2} Nu_r &= Nu = -K_4 \theta'(0) \\ \mathrm{Re}_r^{-1/2} Sh_m &= Sh = -\phi'(0) \end{aligned}\right\} \tag{18}$$

where, Re_r is the local Reynold number.

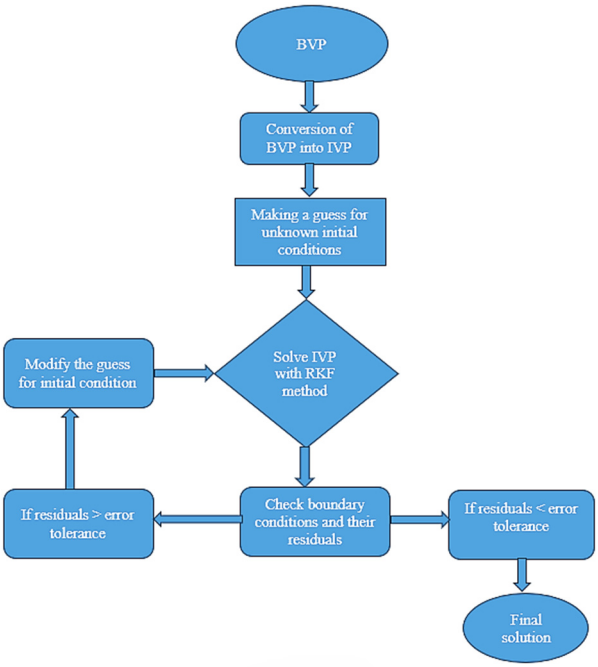

Figure 2. Flow chat for BVP4C

Numerical Technique

The nonlinear ODEs (10–12), subject to the boundary conditions (14), are solved using MATLAB's built-in function of the BVP4C package. This solver for boundary value problems is based on the shooting technique. Due to the highly nonlinear nature of this modified non-dimensional coupled system of equations, finding an accurate solution can be challenging. For equations (10–12), we utilize numerical methods. Introducing new variables into ordinary differential equations (10–12) transforms the highly nonlinear third- and second-order coupled system into a first-order system. Let's proceed with this process by defining the new variables as

$$f = f(1),\ f' = f(2),\ f'' = f(3),\ \theta = f(4),\ \theta' = f(5), \phi = f(6),\ \phi' = f(7)\} \tag{19}$$

The first-order ODEs system is now obtained by substituting these variables into equations (10–12). (Manjunatha et al. [31])

$$\frac{d}{d\eta}\begin{pmatrix} f(1) \\ f(2) \\ f(3) \\ f(4) \\ f(5) \\ f(6) \\ f(7) \end{pmatrix} = \begin{pmatrix} f(2) \\ f(3) \\ \dfrac{(f(2))^2 - f(1)f(3) - K_6\left(\dfrac{Gr}{\mathrm{Re}^2}\right)f(4) + K_7\left(\dfrac{Gm}{\mathrm{Re}^2}\right)f(6) - \dfrac{1}{K_2}\left(K_5 M + K_1 K\right)f(2)}{\left(1+\dfrac{1}{\beta}\right)} \\ f(5) \\ \dfrac{-f(1)f(5) + \dfrac{Q}{\mathrm{Pr}\,K_3}f(4) - \dfrac{Ec}{K_3}\left(K_5 M + K_1 K\right)(f(2))^2 - \left(1+\dfrac{1}{\beta}\right)\dfrac{K_1}{K_3}Ec\,(f(3))^2}{\dfrac{1}{\mathrm{Pr}}\left(\dfrac{K_4}{K_3} + \dfrac{4Rd}{3}\dfrac{1}{K_3}\right)} \\ f(7) \\ Sc\left(-f(1)\phi(7) + Krf(6)\right) \end{pmatrix} \tag{20}$$

RESULTS AND DISCUSSION

The reduced ordinary differential equations from (10-12) ate solved numerically using shooting package through BVP4C package. The numerical results were compared with previous findings and showed good agreement. This section analyzes the impact of relevant parameters using graphs, as illustrated in Figures 3-22. The non-dimensional parameter values chosen for numerical calculations are $M = 1, Gr = 2, Gm = 4, \beta = 1.4, Rd = 0.1, Ec = 0.1, Q = 0.1, \mathrm{Re} = 4,$ $Kr = 1.8, Sc = 0.6, K = 1.2, \mathrm{Pr} = 21$ (kerosene) and $\mathrm{Pr} = 6.8$ (water), and they remain fixed during the present simulation.

The $f'(\eta)$ and $\theta(\eta)$ distributions are influenced by magnetic field parameters, as seen in Figure 3 and 4. The $f'(\eta)$ is influenced by the M, which lowers velocity in both water and kerosene by producing a Lorentz force that opposes the fluid motion as shown in Figure 3. As the M upsurges, the fluid flow slows down due to the resistive force that effect on fluid velocity. Kerosene increases viscosity causes this effect to be more apparent, as it amplifies the viscous force with the magnetic field and damping effects. Figure 4 illustrates that the M impacts the temperature profile $(\theta(\eta))$ for kerosene and water. Heat buildup and a rise in $\theta(\eta)$ result from this decrease in velocity, which limits convective heat transport. Its higher viscosity helps with the impact, which is evident in water because it enhances flow in damping.

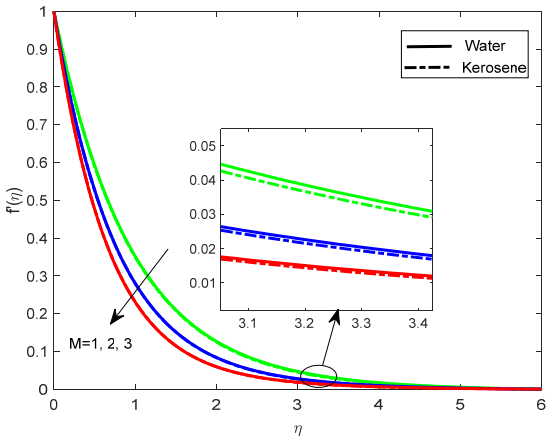

Figure 3. Influence of magnetic field parameter on $f'(\eta)$

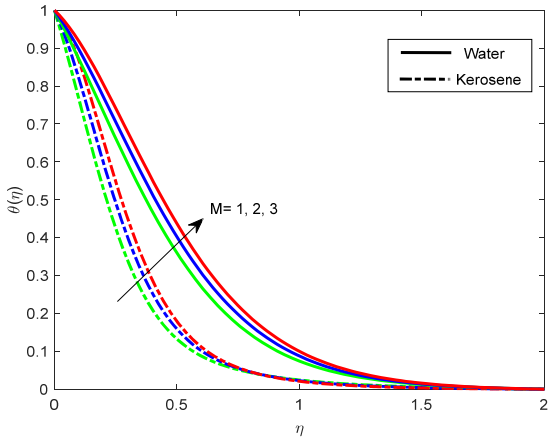

Figure 4. Influence of magnetic field parameter on $\theta(\eta)$

The impact of the on the $\theta(\eta)$ and $f'(\eta)$ is depicted in Figures 5 and 6. The $f'(\eta)$ declines as K increases. As a result, Figure 5 shows that using water as the base fluid causes the velocity boundary layer to decay more rapidly, whereas using kerosene yields a thicker velocity boundary layer. The impact of the porosity parameter on the $\theta(\eta)$ for the base fluids is shown in Figure 6. This figure shows that, when water is used as the base fluid, increasing the porosity parameter K increases the thermal boundary-layer thickness.

Based on Figure 7, the Casson parameter (β) upsurges the flow resistance due to yield stress, which lowers the $f'(\eta)$ in both water and kerosene. This effect is more significant for kerosene than water because of its higher viscosity

and apparent non-Newtonian behavior. The Casson parameter influences the temperature profile $\theta(\eta)$, which controls the fluid's yield stress as depicted in Figure 8. When Casson parameter decreases the heat transfer is enhanced then the temperature profile for both kerosene and water as a base fluid increase. This effect is evident because water has less viscosity and better thermal conductivity.

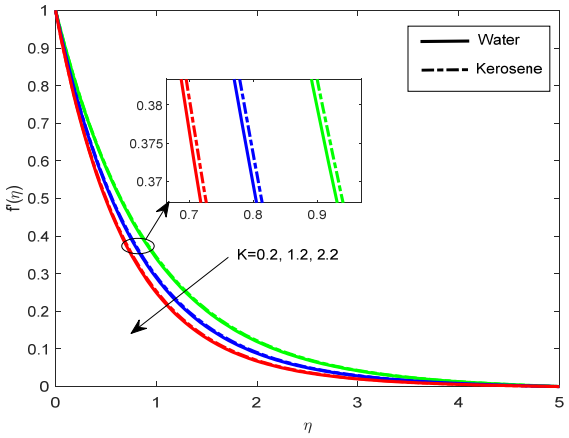

Figure 5. Influence of porosity parameter on $f'(\eta)$

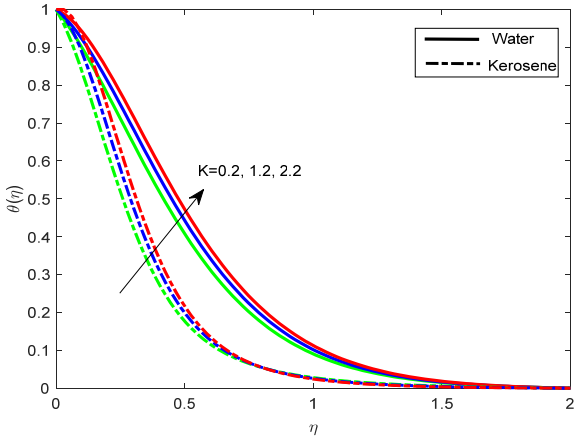

Figure 6. Influence of porosity parameter on $\theta(\eta)$

The effect of the thermal Grashof number (Gr) is shown in Figure 9. The Gr signifies the proportion of buoyant force to viscous force on velocity. For both kerosene and water, as increase in Gr and $f'(\eta)$ increases. Generally, a rise in thermal Grashof causes a surge in buoyancy forces, which raises velocity. In Figure 10, the least value of the solutal Grashof number ($Gm = 2$) has the least effect on the primary flow of water based Casson hybrid nanofluid as compared to kerosene based Casson hybrid nanofluid and gradually rises for a higher value of Gm . These phenomena occurred due to the fact that the buoyancy force driven by solutal differences leads to increases in fluid flow.

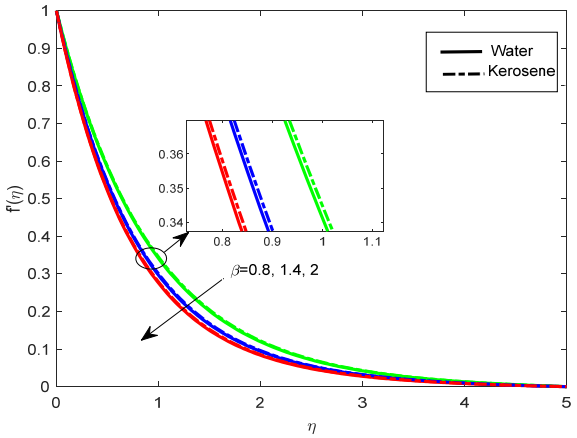

Figure 7. Influence of the Casson parameter on the $f'(\eta)$

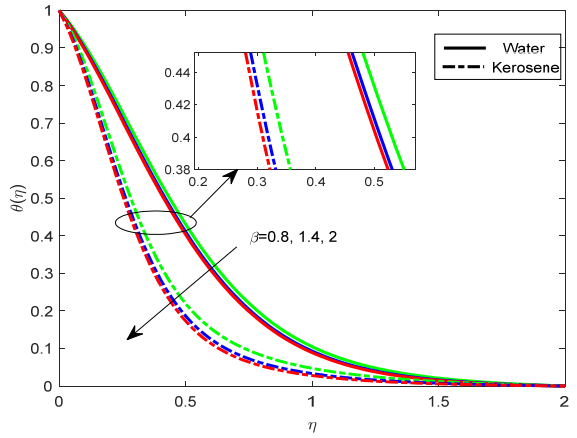

Figure 8. Influence of Casson parameter on $\theta(\eta)$

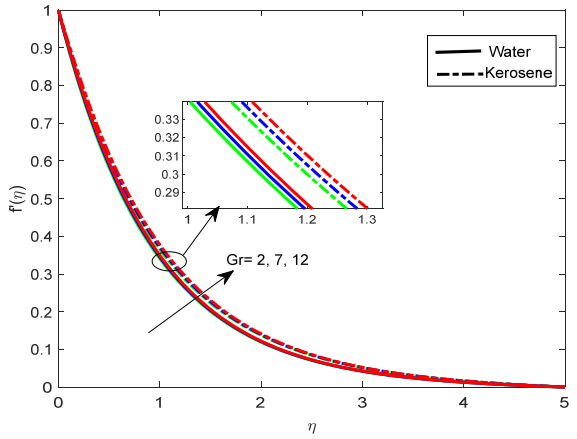

Figure 9. Influence of thermal Grashof number on $f'(\eta)$

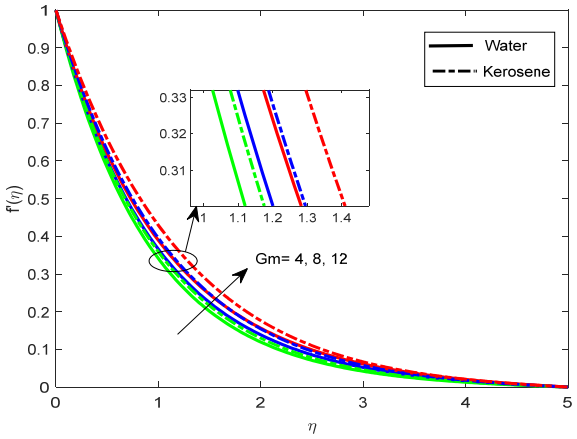

Figure 10. Influence of mass Grashof number on the $f'(\eta)$

Figure 11 shows how the Reynolds number impacts the velocity distribution. For the non-Newtonian fluid (Casson fluid), this figure demonstrates that increasing the Reynolds number causes a drop in velocity over a stretching sheet in both water and kerosene. Figure 12 shows that the radiation parameter (Rd) impacts $\theta(\eta)$.

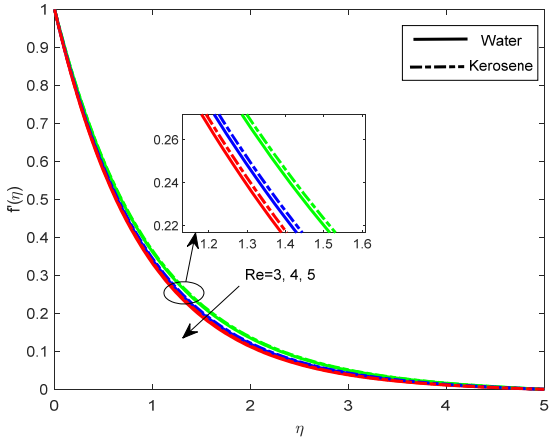

Figure 11. Influence of Reynolds number on $f'(\eta)$

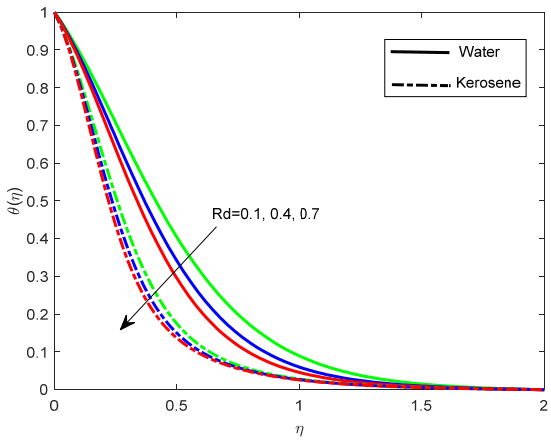

Figure 12. Influence of radiation parameter on $\theta(\eta)$

For a more significant value of Rd the viscosity of the boundary layer declines as the $\theta(\eta)$ increases. For the $Co + Al_2O_3$ /water+kerosene hybrid nanofluid, Rd addresses thermal conduction heat transfer, radiation parameters from a physical point, and its relative immersion of Rd. Thus, warmth is added to the regime for values of the Rd, which enhances $\theta(\eta)$, and Rd enhances the thermal diffusivity of nanofluids. Here, we analyze heat transport in the presence of radiation and talk about forced flow over a stretching sheet. Radiation enhances the effect of heat conductivity. Heat transport is linearly enhanced by radiation.

According to Figure 13, the constant heat source parameter (Q) produces heat in the hybrid nanofluid. By increasing the Q, the $\theta(\eta)$ of the system upsurges in both kerosene and water. As Q rises, the fluid's temperature increases, water heats up more quickly due to its lower specific heat capacity. Kerosene shows a slower rate of temperature increase because of its greater specific heat capacity. The higher heat produces a more prominent thermal boundary layer in both fluids, resulting in a significant temperature difference near the wall. Figure 14 represents the effects of Eckert number on $\theta(\eta)$. When the number of Eckert increases, the viscous dissipation increases, which changes the kinetic energy into thermal energy. The process increases the fluid temperature in water-based and kerosene-based hybrid nanofluids. The temperature at the boundary layer increases as Ec rises due to the conversion of greater velocity-related to energy into heat. Water heat reduces viscosity, making it possible for the temperature to rise more quickly, making the effect more apparent. Kerosene's greater viscosity causes $\theta(\eta)$ to rise while reducing the temperature increase.

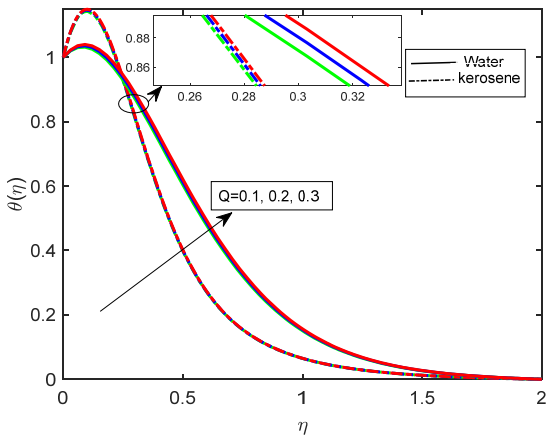

Figure 13. Influence of heat source parameter on $\theta(\eta)$

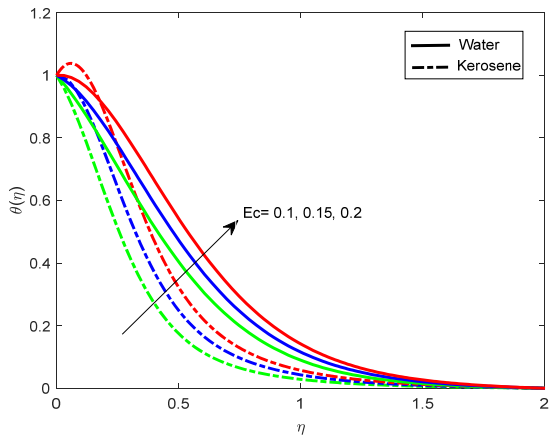

Figure 14. Influence of the Eckert number on $\theta(\eta)$

The effect of Sc on $\phi(\eta)$ is depicted in Figure 15. A rise in the Sc leads to slower mass diffusion, which causes a more uniform concentration distribution. The impact of kerosene base fluid is greater due to the higher viscosity. An increased Schmidt number results in a more steady and less noticeable concentration gradient in both fluids. As shown in Figure 16, the chemical reaction parameter (Kr) suppresses the concentration profile $\phi(\eta)$ in both water and kerosene by enhancing solute absorption. The concentration of the fluid declines significantly as Kr increases due to increase in reaction

rates. Although each fluid's concentration diminishes at varying rates due to its unique transport properties, this phenomenon occurs in both fluids. An elevated Kr yields a more uniform and reduced concentration distribution in both cases.

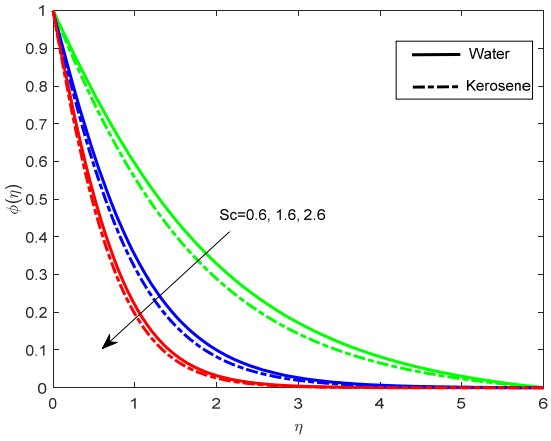

Figure 15. Influence of Schmidt number on $\phi(\eta)$

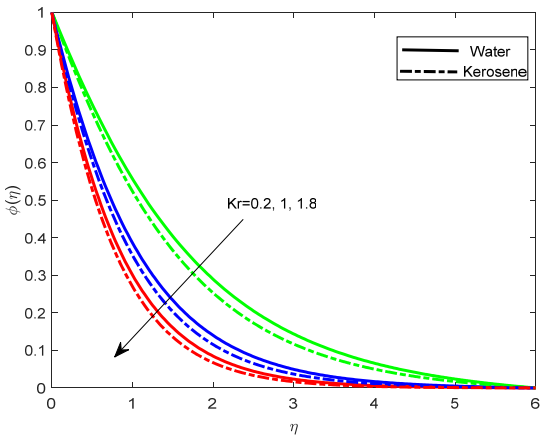

Figure 16. Influence of chemical reaction parameter on $\phi(\eta)$

Response Surface Methodology

The RSM is a valuable technique for creating empirical relationships between a wide range of relevant characteristics. It allows one to look at the input elements with the least and most significant influence on the outputs. RSM aims to maximise replies; this study ascertains how selected input parameters, specifically M , β, and Gm, affect Cf , Q, Ec, and Rd affect Nu, and Kr, Sc affect Sh. Table 3-5 displays the three levels and a specified range of input parameter adjustments. (Manaswini et al. [32])

Table 3: The effects of various parameter values

Parameter	Symbol	Level		
		-1	0	1
$1 \le M \le 3$	W1	1	2	3
$0.8 \le \beta \le 2$	W2	0.8	1.4	2
$4 \le Gm \le 12$	W3	4	8	12

Table 4: The effects of various parameter values

Parameter	Symbol	Level		
		-1	0	1
$0.1 \le Q \le 0.3$	W1	0.1	0.2	0.3
$0.1 \le Ec \le 0.2$	W2	0.1	0.15	0.2
$0.1 \le Rd \le 0.7$	W3	0.1	0.4	0.7

Table 5: The effects of various parameter values

Parameter	Symbol	Level		
		-1	0	1
$0.2 \le Kr \le 1.8$	W1	0.2	1	1.8
$0.6 \le Sc \le 2.6$	W2	0.6	1.6	2.6

In the subsequent stage, a numerical framework comprising 20 simulation runs is developed using the selected input parameters to evaluate the Cf, and Nu as reported in Tables 6 and 7. Additionally, 13 numerical runs are conducted for the chosen parameters, and the corresponding Sh results are presented in Table 8. A second-order polynomial model is employed to represent the relationship between the input variables and the responses. This approach effectively captures the interaction effects among the governing parameters.

Table 6. A CCD-based investigative approach

Run	Code values			Real values			Response	
	W1	W2	W3	M	β	Gm	Cf / Kerosene	Cf / water
1	1	-1	-1	3	0.8	4	1.469513	1.5254
2	0	0	0	2	1.4	8	1.441879	1.502736
3	1	0	0	3	1.4	8	1.613828	1.668639
4	0	0	0	2	1.4	8	1.441879	1.502736
5	-1	1	1	1	2	12	1.256014	1.331229
6	0	1	0	2	2	8	1.533192	1.590474

Run	Code values			Real values			Response	
	W1	W2	W3	M	β	Gm	Cf / Kerosene	Cf / water
7	0	0	-1	2	1.4	4	1.503529	1.556749
8	1	1	1	3	2	12	1.654406	1.713686
9	1	1	-1	3	2	4	1.783811	1.828922
10	0	0	1	2	1.4	12	1.380485	1.448841
11	0	0	0	2	1.4	8	1.441879	1.502736
12	0	-1	0	2	0.8	8	1.275628	1.345393
13	0	0	0	2	1.4	8	1.441879	1.502736
14	1	-1	1	3	0.8	12	1.374032	1.441922
15	0	0	0	2	1.4	8	1.441879	1.502736
16	-1	-1	-1	1	0.8	4	1.168365	1.24209
17	-1	0	0	1	1.4	8	1.441879	1.32327
18	0	0	0	2	1.4	8	1.441879	1.502736
19	-1	1	-1	1	2	4	1.39995	1.456847
20	-1	-1	1	1	0.8	12	1.06423	1.152761

Table 7. A CCD-based investigative approach

Run	Code values			Real values			Response	
	W1	W2	W3	Ec	Q	Rd	Nu /Kerosene	Nu /Water
1	1	1	-1	0.2	0.3	0.1	1.902361	1.379571
2	0	-1	0	0.15	0.1	0.4	0.813153	1.383466
3	0	0	1	0.15	0.2	0.7	1.284033	1.383972
4	0	0	0	0.15	0.2	0.4	0.849009	1.383268
5	0	0	0	0.15	0.2	0.4	0.849009	1.383268
6	0	1	0	0.15	0.3	0.4	0.885069	1.383066
7	-1	1	1	0.1	0.3	0.7	1.902361	1.386893
8	0	0	0	0.15	0.2	0.4	0.849009	1.383268
9	0	0	0	0.15	0.2	0.4	0.849009	1.383268
10	0	0	-1	0.15	0.2	0.1	0.416939	1.382287
11	-1	-1	-1	0.1	0.1	0.1	1.063311	1.384939
12	1	-1	-1	0.2	0.1	0.1	1.834498	1.38002
13	-1	-1	1	0.1	0.1	0.7	0.907105	1.387217
14	0	0	0	0.15	0.2	0.4	0.849009	1.383268
15	1	-1	1	0.2	0.1	0.7	3.383973	1.381126
16	1	0	0	0.2	0.2	0.4	2.66211	1.380437
17	1	1	-1	0.2	0.3	0.1	1.882659	1.379571
18	-1	0	0	0.1	0.2	0.4	0.969722	1.3861
19	-1	1	-1	0.1	0.3	0.1	1.013761	1.384609
20	0	0	0	0.15	0.2	0.4	0.849009	1.383268

Table 8. A CCD-based investigative approach

Run	Code values		Real values		Response	
	W1	W2	Kr	Sc	Sh /Kerosene	Sh /Water
1	-1	-1	0.2	0.6	0.689451	1.502736
2	1	0	1.8	1.6	1.871837	1.530168
3	1	1	1.8	2.6	2.397922	1.540488
4	0	0	1	1.6	1.489013	1.522568
5	0	1	1	2.6	1.909637	1.532369
6	1	-1	1.8	0.6	1.156877	1.513357
7	0	0	1	1.6	1.489013	1.522568
8	0	0	1	1.6	1.489013	1.522568
9	-1	1	0.2	2.6	1.248423	1.51955
10	-1	0	0.2	1.6	0.983639	1.511771
11	0	0	1	1.6	1.489013	1.522568
12	0	0	1	1.6	1.489013	1.522568
13	0	-1	1	0.6	0.943398	1.508495

The created model's practical applications and consequences are validated through the use of Analysis of Variance (ANOVA). For all derived quantities, Table 9-11 indicates that the parameter is significant if the p value is less than 0.05. Conversely, it is not significant otherwise. The interactions M^2, β^2, $M\beta$, $M\,Gm$, and βGm for kerosene, along with Gm^2, $M\,Gm$, for water, are considered non-significant. The R^2 values are 96.67% kerosene and 99.98% water for Cf. Conversely, Q^2, Rd^2, $Q\,Ec$ for kerosene and Q^2, Ec^2, $Q\,Rd$ for water are non-significant. The R^2 values are 98.96%

kerosene and 100.00% water for Nu . The R^2 values are 99.85% kerosene and 99.72% water for Sh , and the relationship with input values (Kr, Sc) demonstrates the model's accuracy.

Table 9. ANOVA of Cf for kerosene and water

Source	DF	Adj SS		Adj MS		F-Value		P-Value		Coeff	
		case-1	case-2	case-1	case-2	case-1	case-2	case-1	case-2	case-1	case-2
Model	9	0.474391	0.466478	0.052710	0.051831	32.28	5864.55	0.000	0.000		
Linear	3	0.443209	0.454167	0.147736	0.151389	90.46	17129.32	0.000	0.000	1.4556	1.50268
M	1	0.244970	0.279683	0.244970	0.279683	150.0	31645.48	0.000	0.000	0.1565	0.167237
β	1	0.162717	0.147281	0.162717	0.147281	99.64	16664.47	0.000	0.000	0.1276	0.121359
Gm	1	0.035522	0.027203	0.035522	0.027203	21.75	3078.01	0.001	0.000	-0.0596	-0.052157
Square	3	0.026768	0.007556	0.008923	0.002519	5.46	285.00	0.017	0.000		
M^2	1	0.007354	0.000121	0.007354	0.000121	4.50	13.71	**0.060**	0.004	0.0517	-0.00664
β^2	1	0.014150	0.003303	0.014150	0.003303	8.66	373.76	0.015	0.000	-0.0717	-0.03466
Gm^2	1	0.003204	0.000000	0.003204	0.000000	1.96	0.01	**0.192**	**0.912**	-0.0341	0.00020
2-Way Interaction	3	0.004415	0.004755	0.001472	0.001585	0.90	179.34	0.474	0.000		
$(M)(\beta)$	1	0.003668	0.004143	0.003668	0.004143	2.25	468.80	**0.165**	0.000	0.0214	0.02276
$(M)(Gm)$	1	0.000067	0.000033	0.000067	0.000033	0.04	3.73	**0.843**	**0.082**	0.0029	0.00203
$(\beta)(Gm)$	1	0.000679	0.000579	0.000679	0.000579	0.42	65.49	**0.533**	0.000	-0.0092	-0.00851
Error	10	0.016331	0.000088	0.001633	0.000009						
Lack-of-Fit	5	0.016331	0.000088	0.003266	0.000018						
Pure Error	5	0.000000	0.000000	0.000000	0.000000						
Total	19	0.490722	0.466567								

Model Summary

S		R-sq		R-sq(adj)		R-sq(pred)	
Case-1	Case-2	Case-1	Case-2	Case-1	Case-2	Case-1	Case-2
0.0404119	0.002972	**96.67%**	**99.98%**	**93.68%**	**99.96%**	76.98%	99.84%

$$Cf = E_0 + E_1 M + E_2 \beta + E_3 Gm + E_{11} M^2 + E_{22} \beta^2 + E_{33} Gm^2 + E_{12} (M)(\beta) + E_{13} (M)(Gm) + E_{23} (\beta)(Gm) \tag{21}$$

$$Cf \,/\, Kerosene = 1.4556 + 0.1565 M + 0.1276 \beta - 0.0596 Gm - 0.0717 \beta^2 \tag{22}$$

$$Cf \,/\, water = \left.\begin{array}{l} 1.50268 + 0.167237 M + 0.121359 \beta - 0.052157 Gm \\ -0.00664 M^2 - 0.03466 \beta^2 + +0.02276 (M)(\beta) - 0.00851 (\beta)(Gm) \end{array}\right\} \tag{23}$$

$$\left.\begin{array}{l} Cf \,/\, Kerosene = 0.0517 M^2 - 0.0341 Gm^2 + 0.0214 (M)(\beta) + 0.0029 (M)(Gm) - 0.0092 (\beta)(Gm) \\ Cf \,/\, Water = 0.00020 Gm^2 + 0.00203 (M)(Gm) \end{array}\right\} \tag{24}$$

Table 10. ANOVA of Nu for Kerosene and Water

Source	DF	Adj SS		Adj MS		F-Value		P-Value		Coeff	
		case-1	case-2	case-1	case-2	case-1	case-2	case-1	case-2	case-1	case-2
Model	9	10.2410	0.000093	1.13788	0.000010	95.47	30461.68	0.000	0.000		
Linear	3	5.1592	0.000086	1.71972	0.000029	144.29	84657.48	0.000	0.000	0.8209	1.38327
Q	1	0.2319	0.000057	0.23192	0.000057	19.46	168346.27	0.001	0.000	0.1782	-0.002797
Ec	1	4.6835	0.000000	4.68350	0.000000	392.97	855.21	0.000	0.000	0.8007	-0.000199
Rd	1	1.8982	0.000005	1.89818	0.000005	159.27	14169.19	0.000	0.000	0.5277	0.000840
Square	3	5.3207	0.000000	1.77358	0.000000	148.81	82.73	0.000	0.000		
Q^2	1	0.0134	0.000000	0.01337	0.000000	1.12	0.00	**0.314**	**0.992**	0.0704	-0.000000
Ec^2	1	2.8980	0.000000	2.89798	0.000000	243.16	0.05	0.000	**0.821**	1.0373	-0.000003
Rd^2	1	0.0139	0.000000	0.01390	0.000000	1.17	153.56	**0.306**	0.000	0.0718	-0.000139
2-Way Interaction	3	1.0014	0.000001	0.33380	0.000000	28.01	537.03	0.000	0.000		
$(Q)(Ec)$	1	0.0028	0.000000	0.00282	0.000000	0.24	20.53	**0.637**	0.001	-0.0227	-0.000036

Source	DF	Adj SS		Adj MS		F-Value		P-Value		Coeff	
		case-1	case-2	case-1	case-2	case-1	case-2	case-1	case-2	case-1	case-2
$(EC)(Rd)$	1	0.2080	0.000000	0.20801	0.000000	17.45	1349.18	0.002	0.000	0.2029	-0.000301
$(Q)(Rd)$	1	0.6846	0.000000	0.68459	0.000000	57.44	0.65	0.000	**0.439**	0.3681	-0.000007
Error	10	0.1192	0.000000	0.01192	0.000000						
Lack-of-Fit	4	0.1190	0.000000	0.02975	0.000000	919.61		0.000			
Pure Error	6	0.0002	0.000000	0.00003	0.000000						
Total	19	10.3601	0.000093								
Model Summary											
S			**R-sq**			**R-sq(adj)**			**R-sq(pred)**		
Case-1	Case-2	Case-1		Case-2		Case-1	Case-2		Case-1		Case-2
0.109171	0.0000184	**98.85%**		**100.00%**		**97.81%**	**99.99%**		76.07%		99.95%

$$Nu = E_0 + E_1 Q + E_2 Ec + E_3 Rd + E_{11} Q^2 + E_{22} Ec^2 + E_{33} Rd^2 + E_{12}(Q)(Ec) + E_{13}(Q)(Rd) + E_{23}(Ec)(Rd) \tag{25}$$

$$Nu / Kerosene = \left.\begin{array}{l} 0.8209 + 0.1782Q + 0.8007Ec + 0.5277Rd \\ +1.0373Ec^2 + 0.2029(Q)(Rd) + 0.3681(Ec)(Rd) \end{array}\right\} \tag{26}$$

$$Nu \text{ /Water} = \left.\begin{array}{l} 1.38327 - 0.002797Q - 0.000199Ec + 0.000840Rd \\ -0.000139Rd^2 - 0.0000036(Q)(Ec) - 0.000301(Ec)(Rd) \end{array}\right\} \tag{27}$$

$$\left.\begin{array}{l} Nu / kerosene = 0.0704Q^2 + 0.07018Rd^2 - 0.0227(Q)(Ec) \\ Nu / Water = -0.00000Q^2 - 0.000139Ec^2 - 0.000007(Q)(Rd) \end{array}\right\} \tag{28}$$

Table 11. ANOVA of Sh for kerosene and water

Source	**DF**	**Adj SS**		**Adj MS**		**F-Value**		**P-Value**		**Coeff**	
		case-1	case-2	case-1	case-2	case-1	case-2	case-1	case-2	case-1	case-2
Model	5	2.46769	0.001237	0.49354	0.000247	953.11	492.65	0.000	0.000		
Linear	2	2.32130	0.001183	1.16065	0.000591	2241.4	1176.99	0.000	0.000	1.48792	1.52254
Kr	1	1.04594	0.000416	1.04594	0.000416	2019.9	827.99	0.000	0.000	0.41752	0.008326
Sc	1	1.27536	0.000767	1.27536	0.000767	2462.9	1526.00	0.000	0.000	0.46104	0.011303
Square	2	0.03008	0.000028	0.01504	0.000014	29.04	28.15	0.000	0.000		
Kr^2	1	0.00912	0.000006	0.00912	0.000006	17.60	12.41	0.004	0.010	-0.0574	-0.001502
Sc^2	1	0.00951	0.000011	0.00951	0.000011	18.36	22.88	0.004	0.002	-0.0587	-0.002040
2-Way Interaction	1	0.11631	0.000027	0.11631	0.000027	224.61	52.97	0.000	0.000		
$(Kr)(Sc)$	1	0.11631	0.000027	0.11631	0.000027	224.61	52.97	0.000	0.000	0.1705	0.002579
Error	7	0.00362	0.000004	0.00052	0.000001						
Lack-of-Fit	3	0.00362	0.000004	0.00121	0.000001						
Pure Error	4	0.00000	0.000000	0.00000	0.000000						
Total	12	2.47131	0.001241								
Model Summary											
S			**R-sq**			**R-sq(adj)**			**R-sq(pred)**		
Case-1	Case-2	Case-1		Case-2		Case-1	Case-2		Case-1		Case-2
0.0227556	0.0007088	**99.85%**		**99.72%**		**99.75%**	**99.51%**		98.51%		97.12%

$$Sh = E_0 + E_1 Kr + E_2 Sc + E_{11} Kr^2 + E_{22} Sc^2 + E_{12}(Kr)(Sc) \tag{29}$$

$$Sh \text{ /kerosene} = \left.\begin{array}{l} 1.48792 + 0.41752Kr + 0.46104Sc - 0.0574Kr^2 \\ -0.0587\,Sc^2 + 0.1705(Kr)(Sc) \end{array}\right\} \tag{30}$$

$$Sh \text{ /water} = \left.\begin{array}{l} 1.52254 + 0.008326Kr + 0.011303Sc - 0.001502Kr^2 \\ -0.002040Sc^2 + 0.002579(Kr)(Sc) \end{array}\right\} \tag{31}$$

Table 12. Comparative table for the current study's different Prandtl numbers.

Pr	Present Study	Ali et al. [21].
0.7	0.45601	0.4560
2.0	0.91332	0.9133

The Shooting method with the bVp4c package is used to solve the non-dimensional equations. Published study validates the current numerical finding for various Prandtl numbers. As the table illustrates, the numerical results are in good accord with the published study.

Figures 17-22 display and provide reference to the residual charts. The mean possibility plots of the residuals indicate exceptional conditions. The observed and fitted values show a significant correlation, as evidenced by the residual diagrams. Kerosene and water as base fluids have the most considerable residuals for the Cf, Nu and Sh.

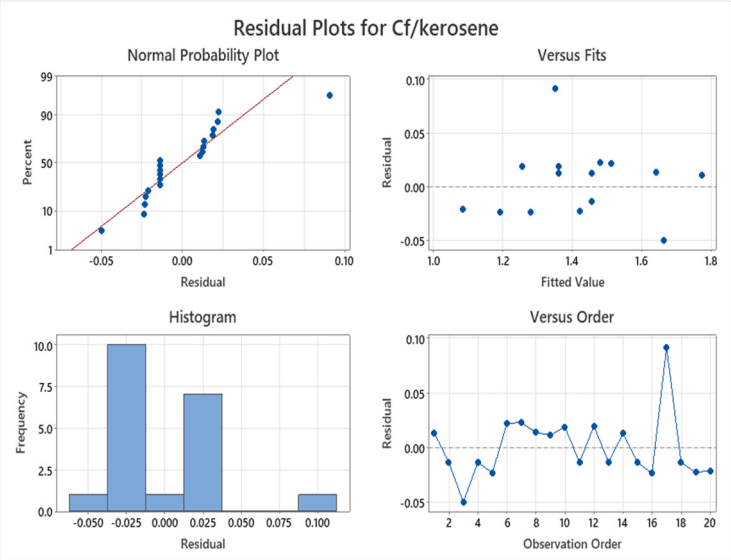

Figure 17. The skin friction coefficient residual plots for the kerosene as a base fluid

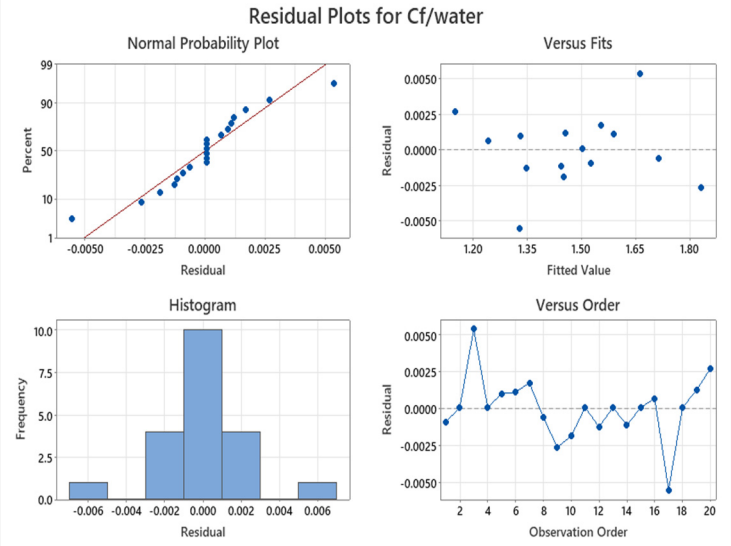

Figure 18. The skin friction coefficient residual plots for water as a base fluid.

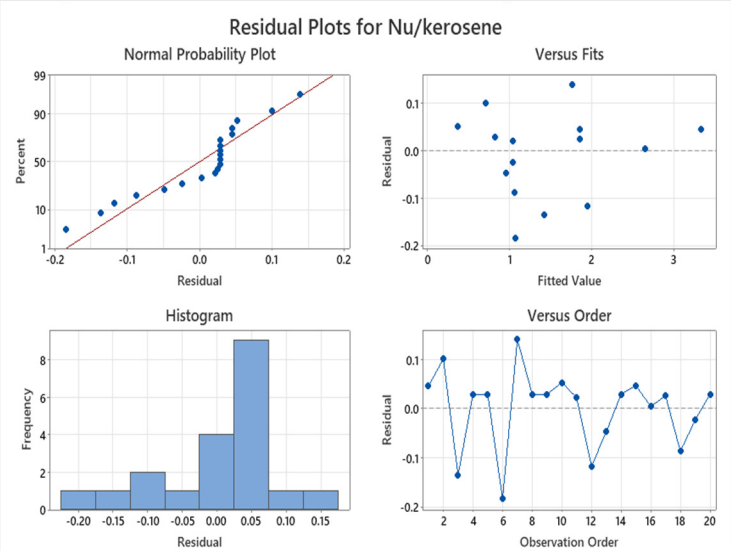

Figure 19. The Nusselt number residual plots for the kerosene as a base fluid.

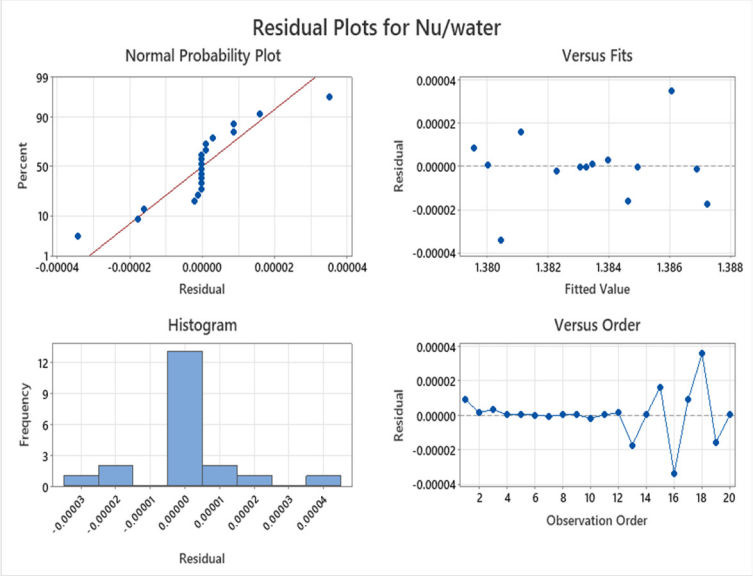

Figure 20. The Nusselt number residual plots for the water as a base fluid.

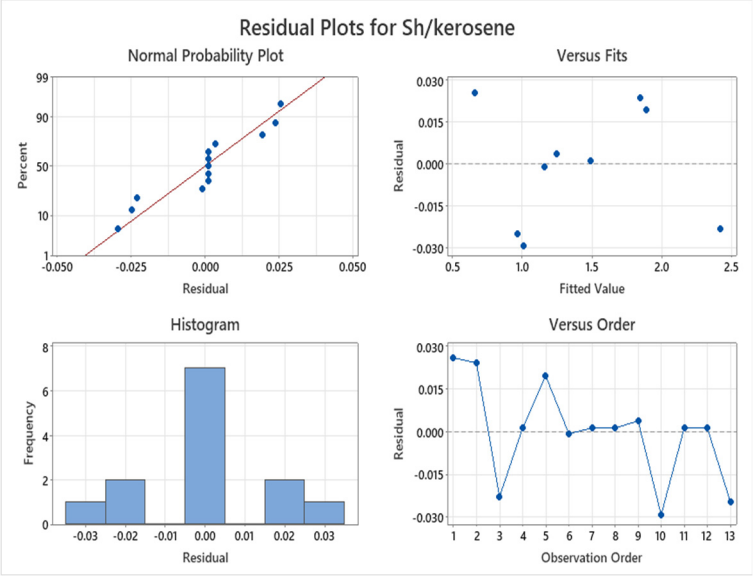

Figure 21. The Sherwood number residual plots for the kerosene as a base fluid

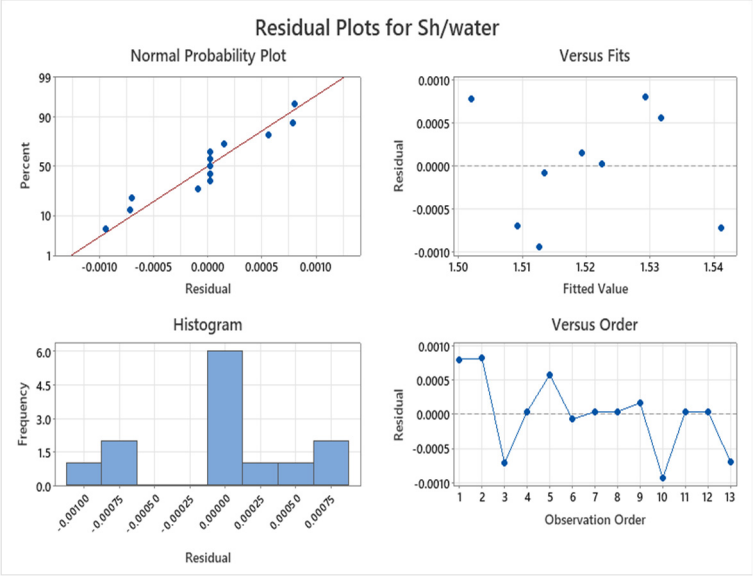

Figure 22. The Sherwood number residual plots for water as a base fluid

The constructed regression models for each response are represented by Equations (21), (25), and (29) in Response Surface Methodology (RSM). Equations (23) and (24) reflect the skin friction regression model, Equations (26) and (27) the Nusselt number model, and Equations (30) and (31) the Sherwood number model. When a word has a statistically significant impact on the answer and its p-value is less than 0.05, it is deemed significant. On the other hand, if a term's p-value is higher than 0.05, it is considered inconsequential and may be the result of random fluctuation. According to the study, several variables in Equations (24) and (28), which represent the skin friction and the Nusselt number, are deemed inconsequential since their p-values are more than 0.05. All factors in the Sherwood number regression model, however, are statistically significant because all p-values are less than 0.05.

Grid Convergence Analysis

To assess the numerical accuracy of this approach, a mesh sensitivity analysis was performed. Figure 23(a) and (b) show the results, with supporting data in **Tables 13a and 13b** for water- and kerosene-based fluids. The computational domain was divided using different grid sizes, and the skin-friction coefficient, Nusselt number, and Sherwood number were calculated. Increasing the number of grid points has very little effect on the calculated values. Changes in Cf, Nu, and Sh are almost unnoticeable once the grid size reaches a moderate level, indicating that making the grid even finer does not change the results. The small differences between grids are confined to the higher decimal places, indicating strong numerical consistency. The graphs in Figure 23(a) and (b) support this finding, as all profiles look almost unchanged with finer grids. This shows that the chosen numerical method yields stable, reliable results for both base fluids. Therefore, a grid size of N = 100 is sufficient to capture the main physics of the problem while keeping the calculations efficient.

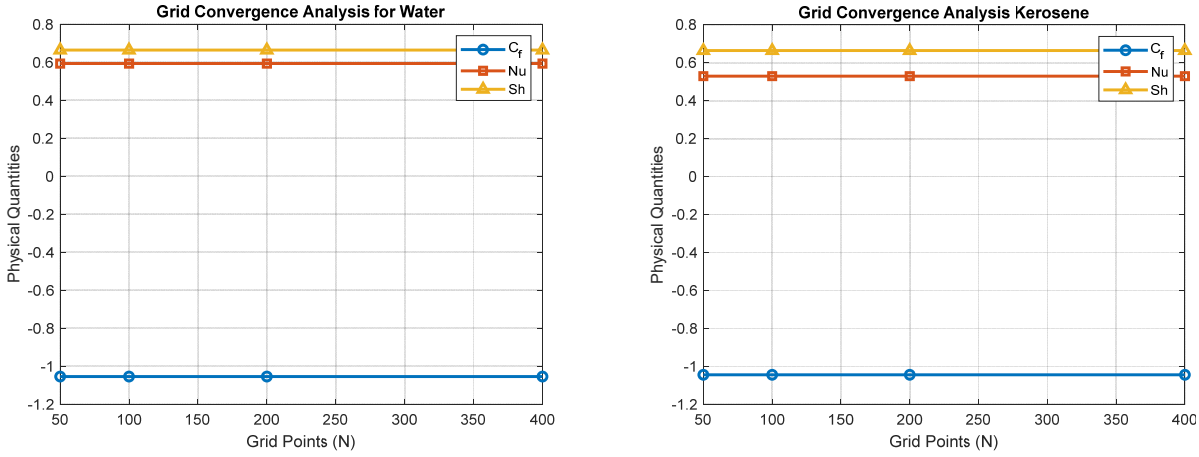

(a) (b)

Figure 23. Grid convergence of Cf, Nu, and Sh for (a) water and (b) kerosene base fluids

Table 13a. Grid convergence results for water-based fluid.

N	*Cf*	*Nu*	*Sh*
50	-1.05421	0.59247	0.66336
100	-1.05421	0.59247	0.66336
200	-1.05421	0.59247	0.66336
400	-1.05421	0.59247	0.66336

Table 13b. Grid convergence results for kerosene base fluid.

N	*Cf*	*Nu*	*Sh*
50	-1.05421	0.59247	0.66336
100	-1.05421	0.59247	0.66336
200	-1.05421	0.59247	0.66336
400	-1.05421	0.59247	0.66336

CONCLUSIONS

This study delves into the numerical analysis of the interaction between hybrid flow ($Al_2O_3 + Co$ /kerosene+water) over a two-dimensional stretching in an imposed magnetic field with the non-Newtonian fluid. This research holds great consequences in hybrid nanofluids, such as kerosene and water, as base fluids. This investigation yields the following noteworthy findings:

- A rise in the M parameter reduces the corresponding $f'(\eta)$ due to the resistance force.
- The Casson fluid parameter decelerates the velocity of the HNF very fast in water compared to kerosene as a base fluid over a stretching sheet.

- The thermal Grashof number (Gr) enhances the $f'(\eta)$ of the fluid in kerosene.
- The heat source and Eckert number escalate water's thermal boundary layer thickness as a base fluid due to the hybrid nano fluid thermal conductivity.
- In the $Al_2O_3 + Co$ /water boosts the radiation parameter, speeds up heat transfer by convection, and raises the suction value, enhancing fluid flow.
- The Casson parameter increases the friction factor rate in a hybrid nanofluid.
- The $\phi(\eta)$ decline significantly as Kr increases due to increased reaction rate.

List of symbols

B_0	Magnetic field strength (A/m)	B_{i1}	Thermal Biot number
Ec	Eckert number	B_{i2}	Concentration Biot-number
Rd	thermal radiation	Gr	Thermal Grashof number
q_r	radiation heat flux	Gm	Mass Grashof number
K	Porosity/permeability	u_w	surface velocity(m/s)
M	magnetic parameter	f	base fluids
Re	Reynold number	nf	nanofluids
Nu_x	Nusselt number	hnf	hybrid nanofluids
x	stream-wise coordinate	k^*	Rosseland approximation
Cf_x	Skin friction coefficient	T_∞	ambient temperature (K)
Sh_x	Sherwood number	$f(\eta)$	dimensionless stream function $f(\eta)$
y	transverse coordinate	$f'(\eta)$	velocity
Q	constant heat generation	η	Dimensionless similarity variable
Sc	Schmidt number	w	surface conditions (near wall)
Kr	Chemical reaction parameter	∞	free stream conditions(ambient)

Data availability

The research reported in the paper did not use any data.

Acknowledgement

I sincerely thank Prof. S. Vijay Kumar Varma for their valuable guidance and constant support throughout this research work.

ORCID

Esara Sivasankar, https://orcid.org/0009-0004-7463-4708; **S. Vijaya Kumar Varma,** https://orcid.org/0000-0002-9757-9316;
M. Sreedhar Babu, https://orcid.org/0000-0001-9880-6253

REFERENCES

[1] L.J. Crane, Z. Angew. Math. Phys. **21**, 645 (1970). https://doi.org/10.1007/BF01587695
[2] N.S. Khashi'ie, N.M. Arifin, R. Nazar, E.H. Hafidzuddin, N. Wahi, and I. Pop, Chin. J. Phys. **64**, 251 (2020). https://doi.org/10.1016/j.cjph.2019.11.008
[3] M. Shoaib, M.A.Z. Raja, M.T. Sabir, S. Islam, Z. Shah, P. Kumam, and H. Alrabaiah, Sci. Rep. **10**, 18533 (2020). https://doi.org/10.1038/s41598-020-75254-8
[4] P. Sreedevi, P. Sudarsana Reddy, and A. Chamkha, SN Appl. Sci. **2**, 1222 (2020). https://doi.org/10.1007/s42452-020-3017-7
[5] I. Waini, A. Ishak, and I. Pop, Appl. Math. Mech. **41**, 507 (2020). https://doi.org/10.1007/s10483-020-2584-7
[6] M. Santhi, K.V.S. Rao, P.S. Reddy, and P. Sreedevi, Heat Transfer **50**, 2929 (2021). https://doi.org/10.1002/htj.22047
[7] S. Dinarvand, M. Yousefi, and A. Chamkha, J. Appl. Comput. Mech. **8**, 11 (2022). https://doi.org/10.22055/JACM.2021.37057.2938
[8] I. Haq, M.F. Yassen, M.E. Ghoneim, M. Bilal, A. Ali, and W. Weera, Symmetry **14**, 1759 (2022). https://doi.org/10.3390/sym14091759
[9] S.A.A. Shah, N.A. Ahammad, E.M.T.E. Din, F. Gamaoun, A.U. Awan, and B. Ali, Nanomaterials **12**, 2174 (2022). https://doi.org/10.3390/nano12132174
[10] S. Elattar, M.M. Helmi, M.A. Elkotb, M.A. El-Shorbagy, A. Abdelrahman, M. Bilal, and A. Ali, Alexandria Eng. J. **61**, 10319 (2023). https://doi.org/10.1016/j.aej.2022.12.013
[11] U. Farooq, A. Jan, and M. Hussain, ZAMM, **104**, e202300306 (2024). https://doi.org/10.1002/zamm.202300306
[12] K. Bhattacharyya, Front. Heat Mass Transf. **4**, 023003 (2013). https://doi.org/10.5098/hmt.v4.2.3003
[13] E. H. Aly and I. Pop, Powder Technol. **367**, 192 (2020). https://doi.org/10.1016/j.powtec.2020.03.026
[14] A. Jamaludin, K. Naganthran, R. Nazar, and I. Pop, Eur. J. Mech. B Fluids **84**, 71 (2020). https://doi.org/10.1016/j.euromechflu.2020.07.003
[15] S. Nandi, B. Kumbhakar, and G. S. Seth, Chin. J. Phys. **77**, 2090 (2022). https://doi.org/10.1016/j.cjph.2022.03.004
[16] A. Rashid, M. Ayaz, S. Islam, A. Saeed, P. Kumam, and P. Suttiarporn, S. Afr. J. Chem. Eng. **42**, 255 (2022). https://doi.org/10.1016/j.sajce.2022.07.009

[17] U. Khan, A. Zaib, A. Ishak, N. C. Roy, S. A. Bakar, T. Muhammad, A. H. Abdel-Aty, and I. S. Yahia, Eur. Phys. J. Spec. Top. **231**, 1195 (2022). https://doi.org/10.1140/epjs/s11734-022-00482-3
[18] S.E. Ghasemi, S. Mohsenian, S. Gouran, and A. Zolfagharian, Results Phys. **32**, 105141 (2022). https://doi.org/10.1016/j.rinp.2021.105141
[19] K. Ali, S. Ahmad, K.S. Nisar, A.A. Faridi, and M. Ashraf, Int. J. Energy Res. **45**, 1 (2021). https://doi.org/10.1002/er.6572
[20] N. A. Zainal, R. Nazar, K. Naganthran, and I. Pop, Neural Comput. Appl. **33**, 11285 (2021). https://doi.org/10.1007/s00521-020-05613-z
[21] T.S. Neethu, A.S. Sabu, A. Mathew, A. Wakif, and S. Areekara, Int. Commun. Heat Mass Transf. **135**, 106115 (2022). https://doi.org/10.1016/j.icheatmasstransfer.2022.106115
[22] S. Nadeem, R.U. Haq, and N.S. Akbar, IEEE Trans. Nanotechnol. **13**, 109 (2014). https://doi.org/10.1109/TNANO.2013.2293735
[23] J. Qing, M.M. Bhatti, M.A. Abbas, M.M. Rashidi, and M.S. Ali, Entropy **18**,123 (2016). https://doi.org/10.3390/e18040123
[24] K.A. Khan, A.R. Butt, and N. Raza, Results Phys. **8**, 610 (2018). https://doi.org/10.1016/j.rinp.2017.12.024
[25] S.M. Abo-Dahab, M.A. Abdelhafez, F. Mebarek-Oudina, and S.M. Bilal, Indian J. Phys. **95**, 2703 (2021). https://doi.org/10.1007/s12648-020-01961-7
[26] N. Hameed, S. Noeiaghdam, W. Khan, B. Pimpunchat, U. Fernandez-Gamiz, M.S. Khan, and A. Rehman, Results Eng. **16**, 100601 (2022). https://doi.org/10.1016/j.rineng.2022.100601
[27] R. Meenakumari, P. Lakshminarayana, K. Vajravelu, and G. Sucharitha, Numer. Heat Transf. A, **83**, 1 (2023). https://doi.org/10.1080/10407782.2023.2175289
[28] R.C.S. Reddy and G. Ramasekhar, East Eur. J. Phys. (4), 286 (2023). https://doi.org/10.26565/2312-4334-2023-4-29
[29] T.N. Tanuja, L. Kavitha, K.U. Rehman, S.V.K. Varma, G.V. Kumar, and Z. Asghar, Int. J. Thermofluids **26**, 101089 (2025). https://doi.org/10.1016/j.ijft.2024.101089
[30] A. Divya, and P.B.A. Reddy, Proc. IMechE Part E, **237**, 196 (2023). https://doi.org/10.1177/09544089221143566
[31] S. Manjunatha, J.S. Kumar, K.U. Rehman, W. Shatanawi, and S.V.K. Varma, Int. J. Thermofluids **26**, 101130 (2025). https://doi.org/10.1016/j.ijft.2024.101130
[32] R. Manaswini, B.N. Hanumagowda, T.N. Tanuja, L. Kavitha, A. Abdulrahman, R.J. Punith Gowda, and S.V.K. Varma, Mod. Phys. Lett. B, **39**(07), 2450420 (2025). https://doi.org/10.1142/S0217984924504207

АНАЛІЗ ТЕРМОМАГНІТНОГО ПОТОКУ ГІБРИДНОЇ НАНОРІДИНИ КАССОНА ЧЕРЕЗ ПОРИСТИЙ ЛИСТ ЩО РОЗТЯГУЄТЬСЯ З ВРАХУВАННЯМ ХІМІЧНОЇ РЕАКЦІЇ З ВИКОРИСТАННЯМ RSM

Есара Сівасанкар[1], М. Срідхар Бабу[1], С. Віджая Кумар Варма[2]
[1]Кафедра прикладної математики, Університет Йогі Вемана, Кадапа, Андхра-Прадеш, 516005, Індія
[2]Кафедра математики, Школа прикладних наук, Дослідницький центр REVA, Університет REVA, Бенгалуру, Карнатака, 560064, Індія

Термофізичний аналіз тепло- та масопередачі має багато потенційних застосувань у сонячних колекторах, хімічних реакторах, медичних пристроях та складних системах охолодження, серед інших застосувань. Завдяки цьому стимулу, у цій роботі часто використовується методологія поверхні відгуку для аналізу тепло- та масопередачі гібридної нанорідини Кассона над проникним розтягуваним листом з конвективними та радіаційними ефектами. Система керування диференціальними рівняннями в похідних похідних, що визначають розроблену модель, перетворюється на зв'язаний набір нелінійних диференціальних рівнянь шляхом застосування відповідних перетворень подібності. Метод стрільби, реалізований за допомогою розв'язувача BVP4c у MATLAB, використовується для чисельного інтегрування цих спрощених рівнянь. Використовуючи табличні дані та графічні представлення, систематично досліджується вплив відповідних фізичних параметрів на розподіли швидкості, температури та концентрації. Крім того, методологія поверхні відгуку використовується для статистичної оцінки ключових змінних відгуку в широкому діапазоні визначальних параметрів, таких як коефіцієнт поверхневого тертя, тепло- та масопередачі. Результати показують, що збільшення параметра Кассона зменшує температурний профіль, оскільки ефективна границя текучості рідини зменшується. Крім того, через збільшення сил Лоренца, сильніше магнітне поле значно зменшує швидкість рідини. Крім того, було помічено, що збільшення об'ємної частки твердої речовини підвищує температуру нанорідини через підвищену теплопровідність. Статистичний аналіз показує, що точність масопередачі для отриманої математичної моделі в гасі становить 99,85%.

Ключові слова: *гібридна нанорідина Кассона; МГД; пористий розтягуваний лист; хімічна реакція; метод відгуку поверхні (RSM)*